Cytometry
PART A
Journal of the International Society for Advancement of Cytometry

Cell Density Modulates Intracellular Mass Transport in Neural Networks

Patricia Cintora,[1] Jyothi Arikkath,[2] Mikhail Kandel,[3] Gabriel Popescu,[3] Catherine Best-Popescu[1]*

[1]Cellular Neuroscience and Imaging Laboratory, Department of Bioengineering, University of Illinois at Urbana-Champaign, 208 North Wright Street, Urbana, Illinois, 61801

[2]Munroe-Meyer Institute, University of Nebraska Medical Center (UNMC), Omaha, Nebraska

[3]Quantitative Light Imaging Laboratory, Department of Electrical and Computer Engineering, Beckman Institute for Advanced Science and Technology, University of Illinois at Urbana-Champaign, Urbana, Illinois, 61801

Received 31 January 2017; Revised 21 March 2017; Accepted 24 March 2017

Grant sponsor: National Science Foundation, Grant numbers: CBET-0939511 STC; DBI 14 − 50962 EAGER; IIP-1353368

Grant sponsor: National Institutes of Health, Grant number: NIH GM108578

Grant sponsor: JA research supported by grants from NIH COBRE, Grant number: 5P20GM103471

Grant sponsor: Alzheimer's Association and Brain and Behavior Research Foundation

Additional supporting information may be found in the online version of this article.

• **Abstract**

In order to fully understand brain connectivity and elucidate the mechanisms involved in central nervous system disease, the field of neuroscience depends on quantitative studies of neuronal structure and function. Cell morphology and neurite (axonal and dendritic) arborization are typically studied by immunohistochemical and fluorescence techniques. However, dry mass content and intracellular mass transport rates have largely been under-investigated given the inherent difficulties in their measurement. Here, spatial light interference microscopy (SLIM) and dispersion-relation phase spectroscopy (DPS) were used to measure pathlength fluctuations that report on the dry mass and transport within cultured primary neurons across low, medium, and high cell density conditions. It was found that cell density (confluence) affects significantly both the growth rate and mass transport. The analysis method is label-free and does not require neuronal tracing, particle tracking, or neuron reconstruction. Since SLIM can upgrade any existing phase contrast microscope and the imaging and analysis are high-throughput, we anticipate that this approach will be embraced by neuroscientists for broad scale studies. © 2017 International Society for Advancement of Cytometry

• **Key terms**

quantitative image analysis; neuron transport rate; quantitative phase imaging; label-free; interferometric microscopy; neuroinformatics

Introduction

Despite great advances in our understanding of neuronal structure and function, our grasp of neuronal dry mass growth and intracellular transport remains limited (1). These properties are difficult to assess, as they require nondestructive imaging over long periods of time (days) and quantitative information (2–5), immunolabeling (2–4), autoradiography (6), viral tracing (7), individual neuronal tracing (3), particle tracking (3), and neuron reconstruction techniques (1,5). To date, what we know about the kinetics of axonal transport comes from decades of radioisotope pulse labeling experiments in laboratory animals (8–10). Such techniques can be labor intensive, time consuming, costly, and generally do not produce the large datasets required for statistical analysis. Nonetheless, dry mass changes and intracellular transport rates are important neuronal properties that merit further investigation as they can provide insight into central nervous system (CNS) development, repair, and disease. Cellular dry mass reflects the non-aqueous content of cells, such as proteins (11), and has been used as a marker for cell growth in time-lapse studies (1,5,11–13). Given that aberrant protein aggregation and accumulation, and defective transport mechanisms are known to play a growing role in numerous neurodevelopmental and neurodegenerative disorders including: Spinal Muscular Atrophy, Amyotrophic Lateral Sclerosis, Parkinson's, and Alzheimer's disease (4,14,15), the development of techniques and instrumentation capable of quantifying changes in neuronal cell mass

ISAC
International Society for Advancement of Cytometry

*Correspondence to: Catherine Best-Popescu, Cellular Neuroscience and Imaging Laboratory, Department of Bioengineering, University of Illinois at Urbana-Champaign, 208 North Wright Street, Urbana, IL 61801, USA. E-mail: cabest@illinois.edu

Published online 00 Month 2017 in Wiley Online Library (wileyonlinelibrary.com)

DOI: 10.1002/cyto.a.23111

© 2017 International Society for Advancement of Cytometry

and intracellular transport dynamics are warranted. Cell mass and growth kinetics have been recognized as critical to cell biology and their accurate measurement identified as an engineering challenge (16). In response to this challenge, Manalis et al. developed a cell weighing method based on cells circulating inside vibrating microcantilevers (17–19). While this technique can be sufficiently accurate for single-cell studies, its application to studying adherent cellular networks is limited.

Recent developments in Quantitative Phase Imaging (QPI) technology (20,21) has enabled researchers to quantitatively study cell structure and dynamics in a label-free mode. Specifically, we use Spatial Light Interference Microscopy (SLIM), a highly sensitive QPI method, to study dry mass growth and kinetics in neural networks (1,11,13,22–27). In order to analyze the spatially and temporally resolved SLIM data, we use Dispersion-Relation Phase spectroscopy (DPS), a method specifically developed for QPI data analysis. We quantify intracellular transport rates simultaneously from multiple cells without the need for tracing or particle tracking. Importantly, our method is applicable for the statistical analysis of large datasets.

We investigated the effects of neuronal plating density (confluency) on cell mass and transport rates. We found consistently higher growth rates in the lower cell density regions. We hypothesize that low cell density plating, such as 30% confluence, results in higher growth rates due to the larger inter-cellular distances that neurites must cover to make new connections. In contrast, high cell density conditions, such as 70% confluence, would display higher overall mass content with decreased cell growth due to contact inhibition. Contact inhibition is the suppression of cell growth following overcrowding, or high confluence plating. In high confluence conditions, cells are more densely distributed such that the somas (cell bodies) are within close proximity of each other. In addition to cell plating density, mass levels may vary due to increased or decreased protein production, variability in protein clearance, or altered cell cycle and cell proliferation.

Intracellular transport is mediated by a combination of both diffusion and active mechanisms that require energy consumption (27–29). For example, most neuronal proteins are synthesized in the soma and require transport through thin structures (axons and dendrites) over long distances (many microns, up to centimeters or meters) such that diffusion is insufficient as a transport mechanism. Thus, active transport is necessary for long-range cargo transport, which is directed along cytoskeletal elements via molecular motors. Based on previous DPS studies of neural networks (23,25), we anticipate that the active transport is dominant. Furthermore, our results indicate that the spread in the velocity distribution is greater for denser networks found in high confluence or increased cell density regions. These findings suggest that in densely packed neuronal networks, mass transport becomes more specialized, with greater variability in cargo speeds.

Materials and Methods

Cell Culture Preparation

Neurons from early postnatal (P0-P1) C57BL/6 mouse cortex were prepared as previously described (30). The animal protocol was approved by the University of Nebraska Medical Center Institutional Animal Care and USE Committee (IACUC). The neurons were plated on 60 mm Poly-D-Lysine coated glass bottom dishes (Cellvis, China). Neurons were seeded at a density of 1×10^6cells/cm^2 in plating media containing 86.55% MEM Eagle's with Earle's BSS (Lonza Inc, Basel Switzerland), 10% Fetal Bovine Serum (re-filtered, heat inactivated; (ThermoFisher Scientific, Inc, Waltham, MA), 0.45% of 20% (wt/vol) glucose, 100 mM sodium pyruvate (Sigma-Aldrich, St. Louis, MO), 200 mM glutamine (Sigma-Aldrich), and Penicillin/Streptomycin (Sigma-Aldrich). A dissociated-cell density gradient throughout the cell plate was obtained by limited mixing of the media and seeded cells. Four hours after plating, unattached cells and debris were removed by replacing the initial medium with fresh maintenance Neurobasal medium (ThermoFisher Scientific) containing B-27 (ThermoFisher Scientific), 200 mM glutamine (Sigma-Aldrich), and Penicillin/Streptomycin (Sigma-Aldrich). Cortical cells were maintained at 37°C in a humidified and 5% CO_2-95% air incubator. Half of the maintenance media was replaced with fresh maintenance media every three days. Our neurons were not immortalized, and did not undergo cell division. Thus, our cell analysis represents changes occurring from the same cells over a period of 29.7 hours.

Spatial Light Interference Microscopy

Images were acquired with our Spatial Light Interference Microscopy (SLIM) system using a Zeiss EC Plan-Neofluar 20×/0.75 N.A objective. The SLIM module (Cell Vista SLIM Pro, Phi Optics, Inc.) is attached to a commercial phase contrast microscope (Axio Observer Z1, Zeiss) as shown in Figure 1a. The SLIM module contains a 4f lens system, and a spatial light modulator (SLM). As the scattered and reference beam intersect at the image plane, the SLM provides four consecutive phase shifts to the reference light beam in increments of $\pi/2$. As a result, four images corresponding to each phase shift ($n\pi/2$, $n = 0, 1, 2, 3$) are recorded sequentially by the CCD camera. The recorded intensity images are then combined to produce one image that yields high contrast quantitative phase maps of the sample. With these phase maps, information about the sample's thickness, density, and refractive index can be extracted in a label-free mode (1,9,13,22–27).

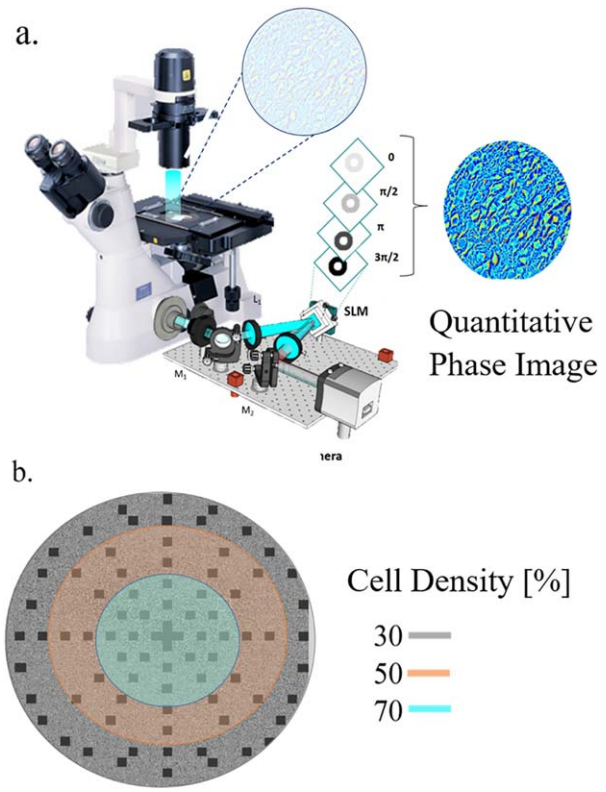

Figure 1. a: Schematics of the spatial light interference microscope (SLIM). SLIM combines conventional phase contrast microscopy (left) and a SLIM module (right). The SLIM module (Cell Vista SLIM Pro, Phi Optics, Inc.) consist of a 4f lens system, and a spatial light modulator (SLM). The SLM produces phase modulation, with phase shifts in increments of $\pi/2$ rad (0, $\pi/2$, π, and $3\pi/2$). The four successive intensity images are taken when the phase of the reference beam is shifted by the SLM. Combining the four images creates a high contrast image. b: Illustration of the different cell density regions (confluence groups) across the cell plate. Postnatal rat cortical neurons were imaged in a 60 mm glass bottom dish every 81 minutes for 29.7 hours. Black squares point to the place where the image stacks of 22 time frames were selected for DPS analysis (70%, $n = 24$; 50% $n = 25$; 30%, $n = 31$) The field of view of a single image stack is 1,024 × 1,024 pixels. [Color figure can be viewed at wileyonlinelibrary.com]

We acquired SLIM images of the mouse cortical neurons in a 60 mm glass bottom dish for 29.7 hours at 81 minute intervals. A total of 899 image stacks, each with 22 time frames, were generated from the scan. Black squares represent image stacks that were systematically selected for DPS analysis at different cell densities (30% confluence, $n = 31$; 50% confluence $n = 25$; and 70% confluence, $n = 24$). Supporting Information Videos [a-c] demonstrate cell growth over 29.7 hour from representative image stacks at 30%, 50%, 70% confluency. The cell confluence of the different plate regions was quantified by estimating total cell area versus the uncovered background area in each field of view. The field of view of a single image stack is 1,024 × 1,024 pixels (see Fig. 1b).

See Supporting Information Figures S1 and S2 for an example of network changes and intracellular transport over time in the high confluency group.

Dispersion-Relation Phase Spectroscopy

Dispersion-relation phase spectroscopy (DPS) measures deterministic and diffusive transport processes within single cells (23,25). The DPS signals exploit path length changes, occurring down to a fraction of nanometer, that are captured by the SLIM system. This sensitivity is based on a previous report where the measurement was done in air versus glass (26). At this time scale, these path length changes are primarily due to intracellular transport in adherent cells. The DPS rates were acquired from multiple cells at a sampling of 1,024 × 1,024 pixels for each of the selected stacks ($n = 80$). We compared intracellular transport rates across the range of plated cell densities (low, medium, and high confluence), within a single plate. The dispersion relation connects the temporal bandwidth, or decay rates, Γ as a function of spatial frequency, q, namely,

$$\Gamma(q) = Dq^2 + \Delta v q \quad (1)$$

In Eq. (1), Δv is the width of the velocity distribution and D is the diffusion coefficient (23).

Thus, the relationship between the decay rate Γ and its wavenumber q represents the dispersion relation associated with mass transport (22).

Results

We examined the average dry mass, the change in mass over time, and the spatial and temporal distribution of active (deterministic) and passive (diffusive) transport processes in neurons under different neuron plating densities. Figure 2 illustrates the three categories of confluence. The dry mass values of individual image stacks were averaged for each confluence group. We used a one-way analysis of variance (ANOVA) to assess overall differences in dry mass means among our three confluence groups. This analysis revealed significant differences among confluency conditions, as shown in Figure 3. A post-hoc Bonferroni test (31) was used with the ANOVA to identify specifically where the significant differences occurred between the three groups. This is because the ANOVA by itself does not specify where the significance occurs between more than two groups. Results of the Bonferroni test showed that the average dry mass value for the high cell density regions, the 70% confluence group [$M = 3{,}517.3$ pg, $SD = 1{,}217$ pg] differed significantly from the medium density regions, the 50% [$M = 2{,}112.5$ pg, $SD = 785.4$ pg] confluency group and the low cell density regions, the 30% [$M = 1555.8$ pg, $SD = 128.9$ pg] confluency group. However, the 30% and 50% confluency groups dry mass values did not differ significantly.

Whole field of view dry mass analysis was conducted over 29.7 hours of imaging measured at 22 time points (see Supporting Information SM1-3 c and S3.). This allowed us to measure the relative change in dry mass over time within each image stack by dividing the dry mass obtained at each time point by the first dry mass value. Growth rates versus confluence are shown in Figure 4. The statistical differences among groups were analyzed using the one-way repeated measure ANOVA (32), with confluence as the within-subject factor.

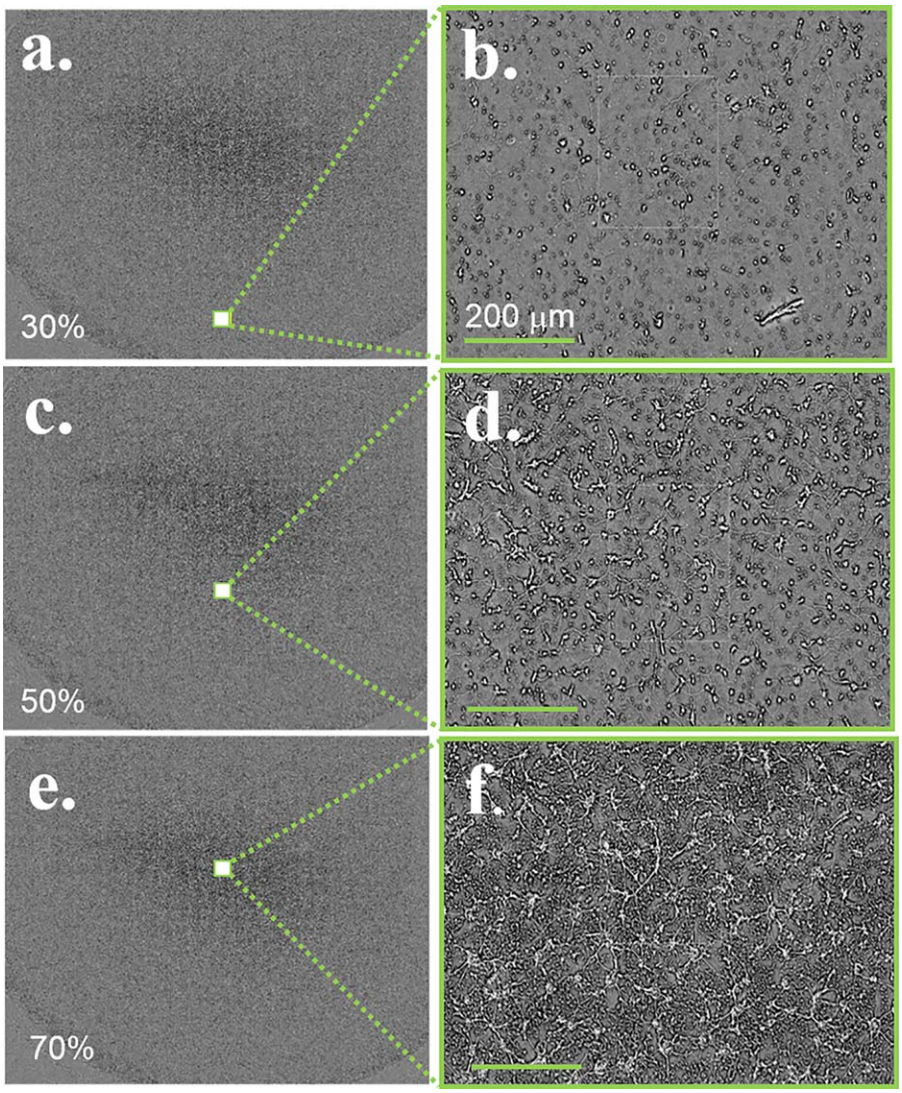

Figure 2. (a–f): Zoom levels across density regions. (a,b) 30%; (c,d); 50%; (e,f) 70% density regions. Objective: Zeiss EC Plan-Neofluar 20×/0.75. [Color figure can be viewed at wileyonlinelibrary.com]

Mauchly's test, which tests the hypothesis that the variances of differences between all combinations of groups are equal (33), indicated that the assumption of sphericity had been violated. Sphericity (ε) refers to the assumption that the relationships between conditions, that is, low confluence and medium confluence, and low confluence and high confluence, in a repeated measures design, are similar or equivalent in variance. In this case, the variance of the differences between low confluence and medium confluence, versus the low and medium confluence and high confluence at different time points were not equal. ANOVAs with repeated measures (within-subject factors) are particularly susceptible to the violation of the assumption of sphericity. Such violation needs to be corrected with the appropriate test which is chosen based on the estimated ε. The ε value is automatically computed in the ANOVA output. Given that our ε was <1, $\varepsilon = 0.53$, we chose the Greenhouse Geisser estimates of sphericity which corrected the degrees of freedom (33). This correction was necessary to produce a more valid critical F-value which reduces the type 1 (false positive) error rate. Following this correction, results demonstrated a significant effect of confluence ($P < 0.001$) see Figure 4. A post-hoc Bonferroni test indicated that growth rate values in the 70% confluence region [$M = 1.0$, $SD = 1.2\text{E-}03$] differed significantly from the 30% [$M = 1.0$, $SD = 4.5\text{E-}03$] and 50% confluency regions [$M = 1.0$, $SD = 3.6\text{E-}03$]. However, low and medium cell density regions, the 30% and 50% confluency groups respectively, were not significantly different from each other (31,32). Our measurements reveal that the overall growth rate decreases consistently with cell density. The 30% confluency group exhibits a growth rate that is 2.3 times faster than the 50% confluency group, which itself grew faster than the 70% confluency group by a factor of 3. Thus, with increasing cell-to-cell contact, the protein synthesis slows down.

Next, we studied the intracellular transport in each group. Figure 5 shows quantitative SLIM phase maps (a, d, g),

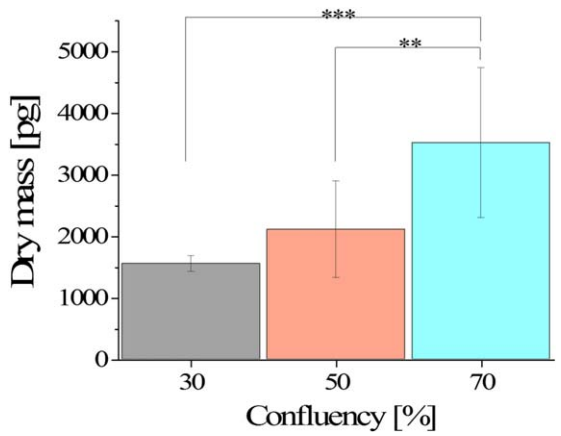

Figure 3. Average dry mass per density group. Dry mass of individual image stacks were averaged for each density group. Statistical analysis was performed via a one-way analysis of variance (ANOVA) with Bonferroni's multiple comparisons post-hoc test. A P value of less than .05 was considered statistically significant. Results indicate that on average, the 70% density group had a significantly higher mass when compared with 50% and 30% density regions. The 50% and 30% density regions did not significantly differ. ** = $P \leq 0.01$, *** = $P \leq 0.001$. [Color figure can be viewed at wileyonlinelibrary.com]

the decay rate versus spatial mode (b, e, h), and the azimuthally-averaged dispersion curve group. The top row represents the data for the low cell density regions the 30% confluency group (a, b, c). The middle row shows data for the medium 50% confluency group (d, e, f) and the bottom row shows data from the high cell density regions the 70% confluency group (g, h, I). A linear curve fit was applied to the dispersion curves at values ranging from 0.32 to 1.32 rad/μm for each of the stacks. The slope values generated via this analysis reflect the spread in velocity of transport processes (see Figs. 5c, 5f, and 5i). This velocity spread, Δv, within the low, medium, and high-confluency groups were analyzed using a one-way ANOVA. Results revealed a significant effect of cell density on Δv (see Fig. 6). The 70% confluency group had the greatest spread in velocity. Post-hoc comparisons using the Bonferroni test indicated that the change in velocity values in the 70% confluency group (high cell density regions) [M = 2.0E-02 μm/min, SD = 2.08E-03 μm/min], the 50% confluency (medium cell density regions) [M = 1.7E-02 μm/min, SD = 3.76E-03 μm/min] and 30% confluency (low cell density regions) [M = 1.4E-02 μm/min, SD = 5.08E-03 μm/min] all differed significantly at $P < 0.05$ (see Fig. 6). These results suggest that, as cell density increases, there is an increase in the diversity of speeds at which cargo is transported, with a higher probability of fast transport.

Summary and Discussion

This study indicates that cortical neuron mass and transport rates vary with plated cell density. As expected, the average dry mass per field of view increased with increasing cell density. This is because, with higher confluency there is a corresponding increase in cell number and number of neurites, and thus dry mass. The growth rate was lower in the high-confluency regions as compared with the low and medium-confluency regions. This suggests that in sparser cultures,

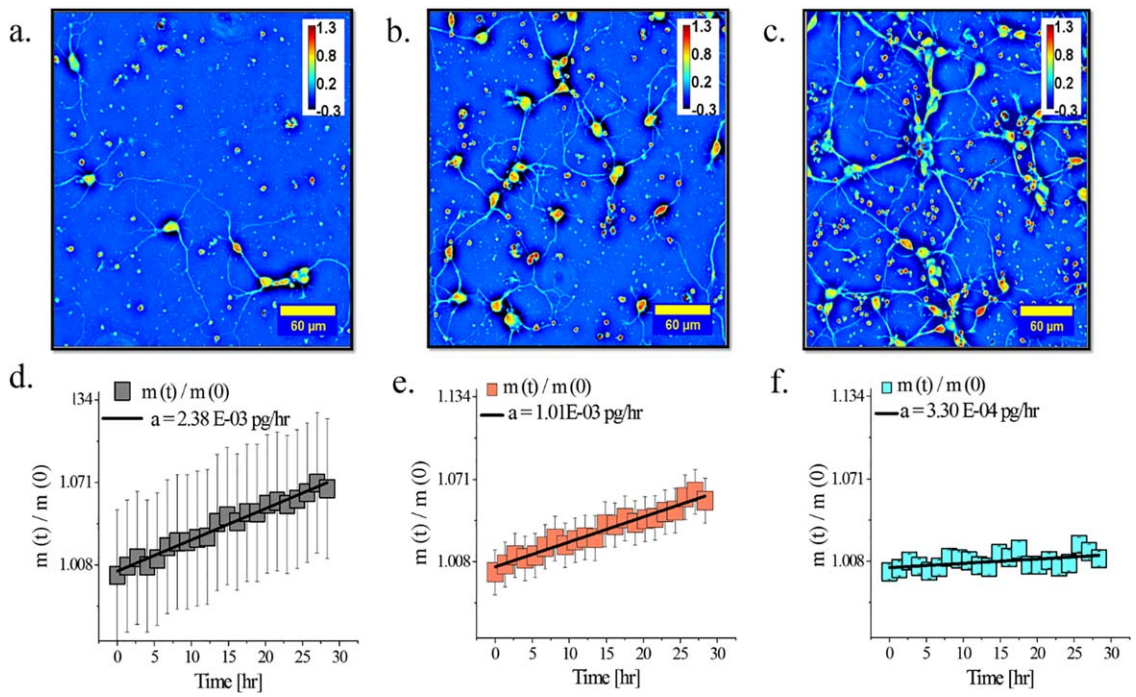

Figure 4. (a–c) SLIM images illustrating representative phase maps in each density group. (d–f) Change in dry mass over 29.7 hours. Whole field of view dry mass analysis was conducted for each image at 22 time frames. Mass growth within the stacks was calculated by dividing the dry mass obtained at each time point by the first value. [Color figure can be viewed at wileyonlinelibrary.com]

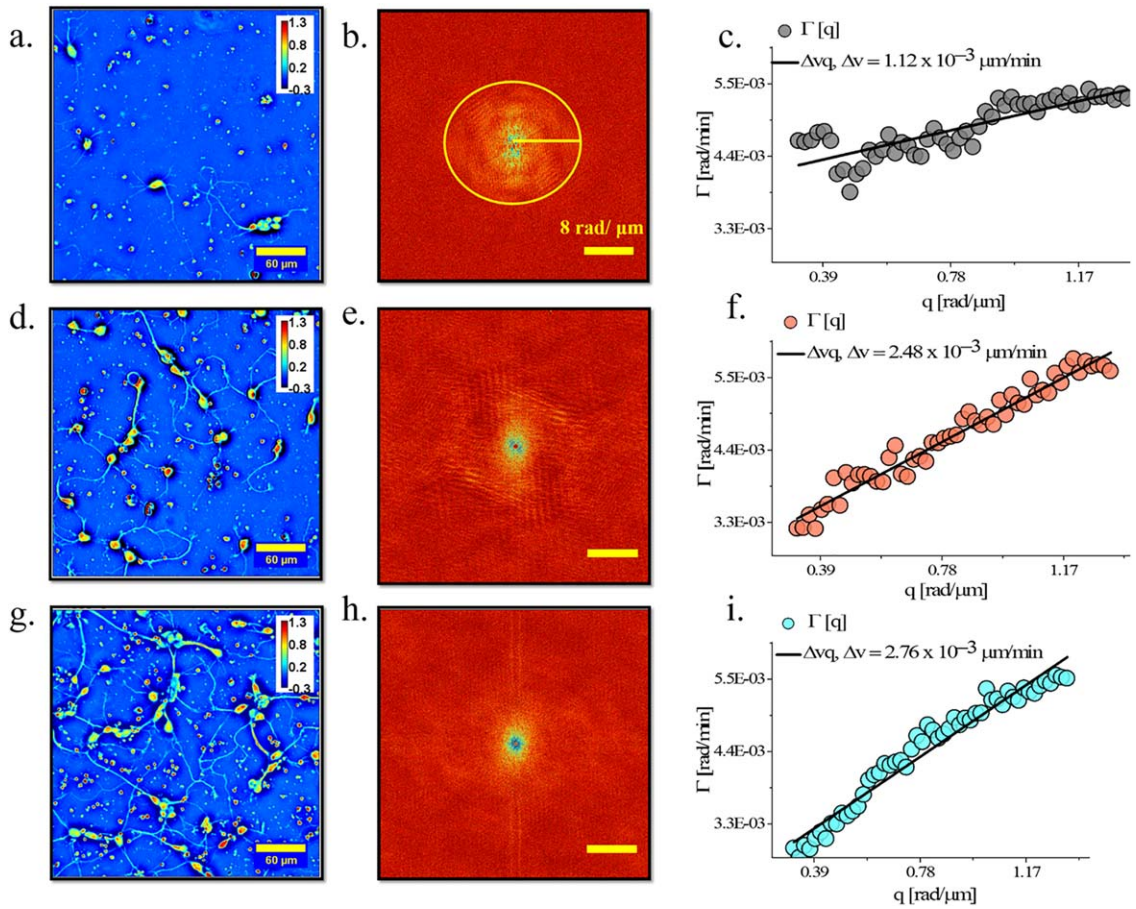

Figure 5. Mass transport analysis. Representative quantitative phase image of a single image stack at (a) 70% (d) 50% and (g) 30% density with their respective dispersion image at (b), (e), and (h). c) Dispersion curve measured for the cells in a. f) Dispersion curve measured for the cells in d. i) Dispersion curve measured for the cells in g. The linear fit indicates directed motion with the slope of the fit indicating velocity spread. [Color figure can be viewed at wileyonlinelibrary.com]

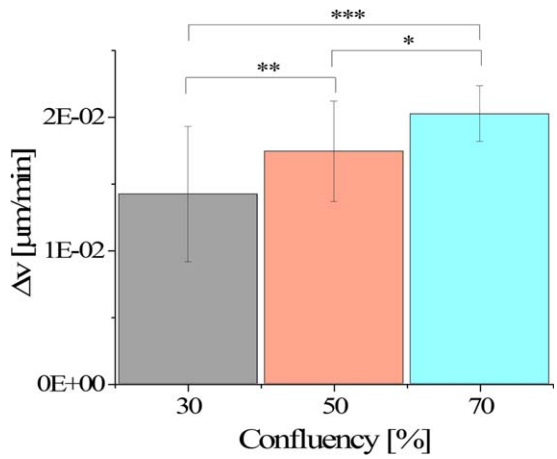

Figure 6. Effects of density on velocity rates. Statistical analysis was performed via a one-way analysis of variance (ANOVA) with Bonferroni's multiple comparisons test to compare image stacks at different densities. A P value of less than 0.05 was considered statistically significant. Results indicate that all groups statistically differed, with velocity rates increasing with increasing density. * = $P \leq 0.05$,** = $P \leq 0.01$, *** = $P \leq 0.001$. [Color figure can be viewed at wileyonlinelibrary.com]

neurons produce more protein to extend neurites over longer distances. Contact inhibition likely plays a role in reducing growth rates for high-confluence regions.

In contrast, the 30% and 50% confluency groups exhibit higher growth rates than the 70% group by a factor of 7 and 2.3, respectively. The slope of the dispersion curves, indicative of the velocity distribution spread, shows that the high-confluency regions exhibit the fastest transport. These findings are consistent with the idea that the long-range cell connections observed in low and medium-density regions are not *replaced* by a greater number of smaller connections in the high-density regions. Instead, in addition to the long-range connections, there is also an abundance of short-range connections, on the order of 10 μm. The speed of transport across the 50 and 70% confluency groups appeared to be similar. This suggests that the same transport mechanism involving microtubules and active motor proteins, for example, kinesin and dynein, are used in transport along dendrites and axons.

In addition to morphometric analysis, a broader analysis that includes dry mass growth and transport rates over time, similar to the one performed here with SLIM and QPI, are warranted and will help move the field of neuroscience

forward. In addition to characterizing altered soma size, cell morphology, neuron number, neurite length and branching properties, quantifying changes in mass and transport rate may help us further understand key mechanisms involved in central nervous system development, repair, and disease. In the future, we plan to delineate anterograde (away from the soma) and retrograde (returning to the soma) transport. The full field-of-view quantitation and long term imaging capabilities of SLIM make it an appealing technique with vast applications in neurobiology

Acknowledgments

We would like to thank Martha Sweeny for all her help with Neuron J training and for all of her insightful comments and suggestions.

Literature Cited

1. Mir M, Wang Z, Shen Z, Bednarz M, Bashir R, Golding I, Prasanth SG, Popescu G. Optical measurement of cycle-dependent cell growth. Proc Natl Acad Sci U S A 2011;108:13124–13129.
2. Burack MA, Silverman MA, Banker G. The role of selective transport in neuronal protein sorting. Neuron 2000;26:465–472.
3. Horton AC, Ehlers MD. Dual modes of endoplasmic reticulum-to-Golgi transport in dendrites revealed by live-cell imaging. J Neurol Sci 2003;23:6188–6199.
4. Misgeld T, Kerschensteiner M, Bareyre FM, Burgess RW, Lichtman JW. Imaging axonal transport of mitochondria in vivo. Nat Methods 2007;4:559–561.
5. Park K, Millet LJ, Kim N, Li H, Jin X, Popescu G, Aluro NR, Hsia KJ, Bashir R. Measurement of adherent cell mass and growth. Proc Natl Acad Sci U S A 2010;107: 20691–20696.
6. Oztas E. Neuronal tracing. Neuroanatomy 2003;2:2–5.
7. Card JP, Rinaman L, Lynn RB, Lee B-H, Meade RP, Miselis RR, Enquist LW. Pseudorabies virus infection of the rat central nervous system: Ultrastructural characterization of viral replication, transport, and pathogenesis. J Neurosci 1993;13:2515–2539.
8. Grafstein B, Forman DS. Intracellular transport in neurons. Physiol Rev 1980;60: 1167–1283.
9. Tytell M, Black MM, Garner JA, Lasek RJ. Axonal transport: Each major rate component reflects the movement of distinct macromolecular complexes. Science 1981;214: 179–181.
10. Brown A. Axonal transport of membranous and nonmembranous cargoes. J Cell Biol 2003;160:817–821.
11. Lee K, Kim K, Jung J, Heo J, Cho S, Lee S, Chang G, Jo Y, Park H, Park Y. Quantitative phase imaging techniques for the study of cell pathophysiology: From principles to applications. Sensors (Basel) 2013;13:4170–4191.
12. Popescu G, Park Y, Lue N, Best-Popescu C, Deflores L, Dasari RR, Feld MS, Badizadegan K. Optical imaging of cell mass and growth dynamics. Am J Physiol Cell Physiol 2008;295:C538–C544.
13. Sridharan S, Mir M, Popescu G. Simultaneous optical measurements of cell motility and growth. Biomed Opt Express 2011;2:2815–2820.
14. Maday S, Twelvetrees AE, Moughamian AJ, Holzbaur EL. Axonal transport: Cargo-specific mechanisms of motility and regulation. Neuron 2014;84:292–309.
15. Roy S, Zhang B, Lee VM, Trojanowski JQ. Axonal transport defects: A common theme in neurodegenerative diseases. Acta Neuropathol 2005;109:5–13.
16. Tzur A, Kafri R, LeBleu VS, Lahav G, Kirschner MW. Cell growth and size homeostasis in proliferating animal cells. Science 2009;325:167–171.
17. Burg TP, Godin M, Knudsen SM, Shen W, Carlson G, Foster JS, Babcock K, Manalis SR. Weighing of biomolecules, single cells and single nanoparticles in fluid. Nature 2007;446:1066–1069.
18. Godin M, Delgado FF, Son S, Grover WH, Bryan AK, Tzur A, Jorgensen P, Payer K, Grossman AD, Kirschner MW, et al. Using buoyant mass to measure the growth of single cells. Nat Methods 2010;7:387–390.
19. Grover WH, Bryan AK, Diez-Silva M, Suresh S, Higgins JM, Manalis SR. Measuring single-cell density. Proc Natl Acad Sci U S A 2011;108:10992–10996.
20. Popescu G. Quantitative Phase Imaging of Cells and Tissues. New York: McGraw Hill; 2011. 385.
21. Marquet P, Depeursinge C, Magistretti PJ. Review of quantitative phase-digital holographic microscopy: Promising novel imaging technique to resolve neuronal network activity and identify cellular biomarkers of psychiatric disorders. Neurophotonics 2014;1:020901.
22. Wang Z, Chun IS, Li X, Ong ZY, Pop E, Millet L, Gillette M, Popescu G. Topography and refractometry of nanostructures using spatial light interference microscopy. Opt Lett 2010;35:208–210.
23. Wang R, Wang Z, Millet L, Gillette MU, Levine AJ, Popescu G. Dispersion-relation phase spectroscopy of intracellular transport. Opt Express 2011;19:20571–20579.
24. Wang Z, Millet L, Mir M, Ding H, Unarunotai S, Rogers J, Gillette MU, Popescu G. Spatial light interference microscopy (SLIM). Opt Express 2011;19:1016–1102.
25. Wang Z, Millet L, Chan V, Ding H, Gillette MU, Bashir R, Popescu G. Label-free intracellular transport measured by spatial light interference microscopy. J Biomed Opt 2011;16:026019.
26. Kim T, Zhou R, Mir M, Babacan SD, Carney PS, Goddard LL, Popescu G. White-light diffraction tomography of unlabeled live cells. Nat Photon 2014;8:256–263.
27. Brangwynne CP, Koenderink GH, MacKintosh FC, Weitz DA. Cytoplasmic diffusion: Molecular motors mix it up. J Cell Bio 2008;183:583–587.
28. Brangwynne CP, Koenderink GH, MacKintosh FC, Weitz DA. Intracellular transport by active diffusion. Trends Cell Biol 2009;19:423–427.
29. MacKintosh FC, Schmidt CF. Active cellular materials. Curr Opin Cell Biol 2010;22: 29–35.
30. Beaudoin MJG, Lee SH, Singh D, Yuan Y, Ng Y, Reichardt LF, Arikkath J. Culturing pyramidal neurons from the early postnatal mouse hippocampus and cortex. Nat Protoc 2012;7:1741–1754.
31. Kim HY. Statistical notes for clinical researchers: Post-hoc multiple comparisons. Restor Dent Endod 2015;40:172–176.
32. Gueorguieva R, Krystal JH. Move over anova: Progress in analyzing repeated-measures data and its reflection in papers published in the archives of general psychiatry. Arch Gen Psychiatry 2004;61:310–317.
33. Greenhouse SW, Geisser S. On Methods in the analysis of profile data. Psychometrika 24:95–112.